RESEARCH ARTICLE

3D reconstruction of the flow and vortical field in a rotating sharp "U" turn channel

Mauro Gallo · Tommaso Astarita

Abstract Particle image velocimetry experiments have been carried out to obtain visualizations and measurements of the main and secondary flow fields in a square channel with a sharp "U" turn. Both the main and the secondary flow fields have been used to perform a 3D reconstruction of the mean flow and vortical fields in the turn region and in the outlet duct. In order to study the influence of the rotation, tests both in stationary (absence of rotation, $Re = 20,000$) and in rotating ($Re = 20,000$ and $Ro = 0.3$) conditions have been performed. The results show that the Coriolis and centrifugal forces, caused by the rotation, yield strong modifications to the symmetrical flow and vortical fields that are generated, in the static case, only by the abrupt inversion of the flow direction.

Abbreviations

3D	Three-dimensional
CCD	Charge-coupled device
LASER	Light amplification by stimulated emission of radiation
LDA	Laser doppler anemometry
Nd:YAG	Neodymium yttrium aluminium garnet

M. Gallo (✉)
Institute of Fluid Dynamics, ETH Zürich, Sonneggstrasse 3, 8092 Zürich, Switzerland
e-mail: gallo@ifd.mavt.ethz.ch

T. Astarita
DIAS, University of Naples "Federico II", p.le Tecchio 80, 80125 Naples, Italy

PIV	Particle image velocimetry

List of symbols

C	Circuit used to the evaluation of the vorticity components
D	Channel hydraulic diameter
$\underline{l}$	Direction normal to the planar surface S
Re	Reynolds number
Ro	Rotation number
S	Planar surface bounded by the circuit C
U	Fluid mean velocity
u, v, w	Mean velocity components
u', v'	Turbulence intensity
u^*	Wall friction velocity
u_1, w_1	Mean velocity components obtained from the images acquired with the rotating channel ($Re = 20,000$, $Ro = 0.3$)
u_2, w_2	Mean velocity components obtained from the images acquired with the rotating channel and the fluid at rest
U_2, W_2	Velocity components of V_{pp}
u_g, v_g, w_g	Mean velocity components relative to the 3D grids
$\underline{V}$	Local velocity vector
V	Local velocity module
V_{pp}	Rotation peripheral velocity relative to the generic point of the investigated plane
W_{2m}	Spatial average of the mean (in time) velocity component w_2 distribution obtained from the images acquired with the rotating channel and with the fluid at rest
x, y, z	Cartesian spatial coordinates
x_c, z_c	Cartesian spatial coordinates of the channel rotation centre
α	Rotation angle

λ_2	Second eigenvalue of the sum of the strain and rotation square tensor
μ	Dynamic viscosity coefficient of the fluid
ρ	Mass density of the fluid
ω	Channel rotational speed
Ω	Local vorticity module
Ω_l	Vorticity components relative to the l direction
$\Omega_x, \Omega_y, \Omega_z$	Mean vorticity components

1 Introduction

In order to improve the thermodynamic efficiency of modern gas turbine engines, it is needed to increase the gas entry temperature. This determines an increase in the heat loads on the early turbine stages. Therefore, to assure the life goals of the turbine blades, it is necessary to cool them both externally, by means of a film cooling imposed on their external surface, and internally, through forced internal convection. In the latter case, the cooling air passes through straight ducts connected by 180° turns present into the blade interior. The presence of these turns and the effects due to the rotation promote the formation of very complex turbulent flows inside the cooling channels, whose knowledge is of fundamental importance for the understanding of the spatial distributions of the convective heat transfer coefficient present in the literature.

In stationary conditions (absence of rotation), many studies of the flow fields present in smooth channels with a 180° sharp turn have been carried out with various visualization and measurement techniques. Kiml et al. (1998), using paraffin mist as a tracer, visualized in laminar regime, in the turn and in the outlet duct, the three-dimensional flow structures generated by the bend. Arts et al. (1992) and Iacovides et al. (1999) performed, by means of laser doppler anemometry (LDA), quantitative measurements of the main flow field, while Liou and Chen (1999a), with the same experimental technique, measured the secondary flow field in the turn region and in the outlet duct immediately after the inversion. Particle image velocimetry (PIV) experiments have been performed by Son et al. (2002) with the aim of studying the high-Reynolds number turbulent flow and wall heat transfer characteristics. Schabacker et al. (1998), by means of a stereoscopic digital PIV system, measured all three velocity components simultaneously.

Numerical analyses of the flow field evolution inside a channel with a 180° sharp turn are also present in literature. Wang and Chyu (1992) obtained information about the three-dimensional flow field for three different geometric configurations of the turn solving the Navier–Stokes equations. Su et al. (2004) studied numerically the effects

caused by the Reynolds number, aspect ratio and buoyancy on both the heat transfer and the flow field.

A large number of works analyzed the flow field in channels with a 180° sharp turn in the presence of rotation in order to simulate the motion of coolant in internal passages of the rotating blades of modern gas turbine. Cheah et al. (1996) performed velocity field measurements, using LDA, in a rotating U-duct of strong curvature with the axis of rotation parallel to the axis of curvature. With the same technique, Iacovides et al. (1999) and Liou and Chen (1999b) measured the turbulent flow field in a square ended U-bend with the axis of rotation orthogonal to the axis of the curve and performed measurements of the local heat transfer coefficient with the aim of identifying possible correlations. Brossard et al. (2005) conducted PIV experiments in a channel with geometry similar to the ones used in the two last cited works and analyzed the flow field in planes parallel to the dividing wall and orthogonal to the axis of rotation.

Numerical analyses of the flow field evolution and of the heat transfer distribution for rotating channels with a 180° sharp turn have been also performed. Al-Qahtani et al. (2002) investigated the effects of rotation, turn and channel orientation with respect to the axis of rotation on the flow field and on the heat transfer distributions. Su et al. (2004) analysed the effects of channel aspect ratio, Reynolds number and buoyancy, on flow behaviour and on heat transfer. Murata and Mochizuki (2004) studied how the interaction of secondary flows, induced by the sharp turn and Coriolis force, affects heat transfer. Iacovides et al. (1996) and Iacovides and Raisee (1999) studied the mean and turbulent flow in rotating U-ducts of strong curvature, with the axis of rotation parallel to the axis of curvature. Kim et al. (2007) performed a numerical simulation using the commercial software FLUENT 6.1 with the aim of getting detailed information about the main and the secondary flow fields.

The main objective of the present work is to perform accurate measurements of the mean flow fields in a channel with a sharp "U" turn by means of the PIV technique and to realize a three-dimensional (3D) reconstruction of the mean flow and of the vortical fields. This should be useful both to improve the understanding of these complex flows and to justify the spatial distributions of the convective heat transfer coefficient present in the literature. Moreover, this study may be also relevant to validate computer programs used to study these complex 3D flows.

The experimental set-up used to perform the measurements is described in the next section, which is followed by a description of the strategy used to reconstruct the 3D flow field. The experimental results, for both the static and the rotating case, are described in the Sect. 4. Finally the conclusions are drawn.

2 Experimental set-up and technique

2.1 Description of the experimental apparatus

The experimental apparatus is shown in Fig. 1. A Plexiglas two-pass channel with a sharp "U" turn is mounted on a revolving platform that is connected to an electric motor by a transmission belt. The electric motor is fed by an inverter so that the platform rotational speed can be varied in a continuous way in the range 0–60 rpm.

The channel, sketched in Fig. 2, has a square cross section of 60 mm (D) on a side, and the central partition wall, which divides the two adjacent ducts, is 12 mm thick. In Fig. 2, it is also highlighted the test region that is formed by the "U" turn and by the portions of the inlet and outlet ducts; both the ducts have a length of 120 mm ($2D$). Since the length of the inlet duct ahead of the measurement zone
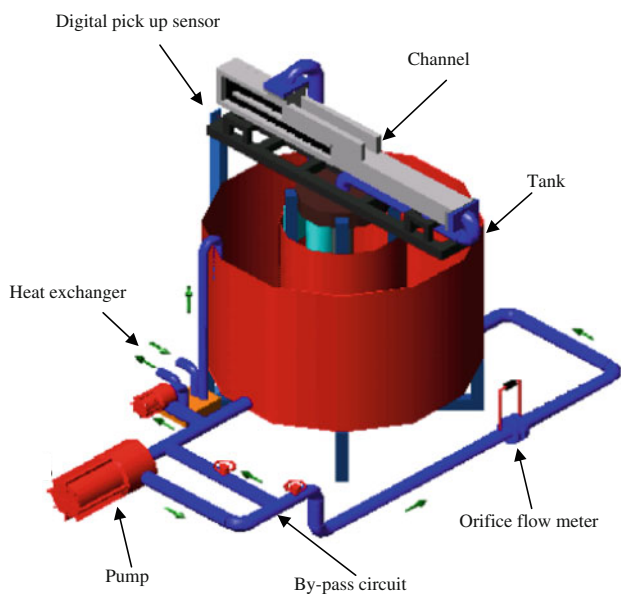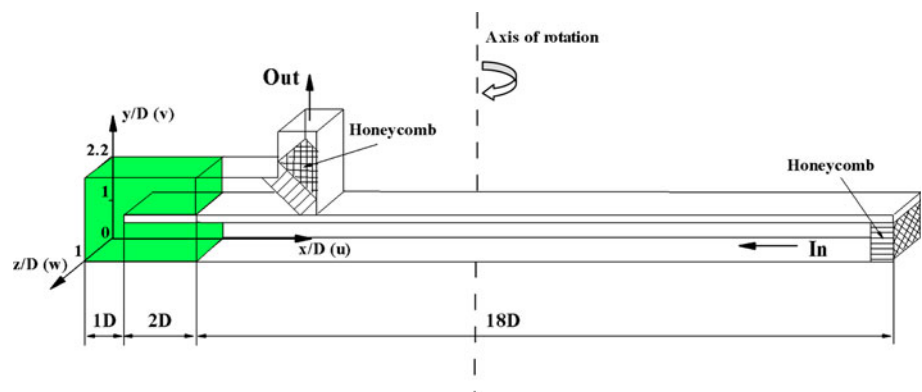

Fig. 1 Sketch of the experimental apparatus

is 1,080 mm ($18D$), the flow can be considered as almost hydro-dynamically fully developed at the entry section of the test region. With the aim to damp the velocity components normal to the main flow direction, a honeycomb layer is inserted at the inlet section. The outlet duct has a length of 240 mm and ends with a 90° turn, which conveys the fluid in the discharging pipe. To attenuate the eventual disturbances produced upstream by the turn, a honeycomb layer is positioned with an inclination angle of 45° with respect to the direction of the main flow.

In order to synchronize the rotating channel with the PIV acquisition system, a digital magnetic pickup sensor is used, and the signal provided by this detector is also used to continually monitor the value of the angular speed.

Water, which is used as a working fluid, is extracted from a tank by a pump (Fig. 1) and then passes through an orifice meter that monitors the flow rate, a rotating hydraulic coupling and finally, after flowing in the test channel, is discharged back in the tank. The water mass flow rate can be regulated in a continuous way with a by-pass circuit, and the water temperature in the tank is kept constant by means of a control circuit and a heat exchanger.

2.2 PIV measurements and technique

The relevant dimensionless numbers are the *Reynolds number Re* and the *Rotation number Ro* (which is the inverse of the *Rossby number*):

$$Re = \frac{\rho U D}{\mu} \tag{1}$$

$$Ro = \frac{\omega D}{U} \tag{2}$$

where D is the channel hydraulic diameter, U is the fluid mean velocity, ω is the channel rotational speed, ρ and μ are the mass density and the dynamic viscosity coefficient of the fluid, respectively. The Reynolds number governs the static behaviour of the flow field in the channel, while
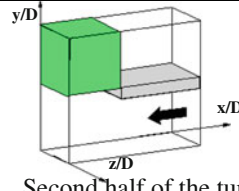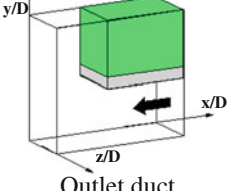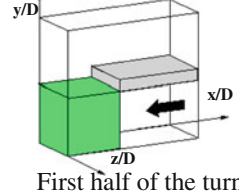
Fig. 2 Test channel

Table 1 Nomenclature of the channel walls

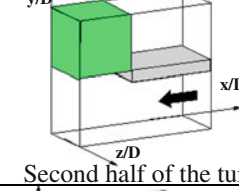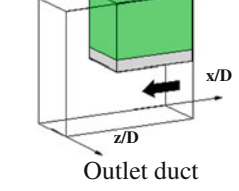| Plane	Name
Static case	
$z/D = 0$	Side wall
$z/D = 1$	Side wall
$x/D = 0$	Frontal wall
$y/D = 0$	External wall
$y/D = 2.2$	External wall
Rotating case	
$z/D = 0$	Leading wall
$z/D = 1$	Trailing wall
$x/D = 0$	Frontal wall
$y/D = 0$	External wall
$y/D = 2.2$	External wall

Ro is a dimensionless measure of the Coriolis effects. The maximum error on Reynolds number and Rotation number evaluation is lower than $\pm 2\%$ (Kline and McClintok 1953). The experimental tests have been performed, for the static case at $Re = 20,000$, while for the rotating case at $Re = 20,000$ and $Ro = 0.3$.

On the basis of the adopted coordinate system (Fig. 2), Table 1 resumes the nomenclature of the channel walls used to describe, in Sect. 4, the flow fields.

To reconstruct and analyze the 3D, flow fields in the turn region and in the outlet duct, PIV measurements have been performed in planes parallel to the three coordinate planes (xy, yz, zx). Table 2 reports all the investigated planes in the turn region and in the outlet duct for both the static and the rotating cases.

Table 2 Investigated planes (static and rotating case)

Static case					
Test region	**Plane**	**# vectors**	**From**	**To**	**Pitch**
Second half of the turn	xy	34x34	z/D=0.03	z/D=0.97	0.03D
	yz	75x75	x/D=0.08	x/D=1	0.17D
	zx	75x75	y/D=1.2	y/D=2.03	0.17D
Outlet duct	xy	84x34	z/D=0.03	z/D=0.97	0.03D
	yz	75x75	x/D=1	x/D=3	0.17D
	zx	174x76	y/D=1.28	y/D=1.37	0.08D
			y/D=1.37	y/D=2.03	0.17D
			y/D=2.03	y/D=2.11	0.08D
Rotating case					
Test region	**Plane**	**# vectors**	**From**	**To**	**Pitch**
First half of the turn	xy	34x34	z/D=0.08	z/D=0.92	0.08D
	yz	75x75	x/D=0.17	x/D=1	0.17D
	zx	75x75	y/D=0.17	y/D=1	0.17D
Second half of the turn	xy	34x34	z/D=0.08	z/D=0.92	0.08D
	yz	75x75	x/D=0.17	x/D=1	0.17D
	zx	75x75	y/D=1.2	y/D=2.03	0.17D
Outlet duct	xy	84x34	z/D=0.08	z/D=0.92	0.08D
	yz	75x75	x/D=1	x/D=2.5	0.17D
	zx	124x74	y/D=1.28	y/D=1.37	0.08D
			y/D=1.37	y/D=2.03	0.17D
			y/D=2.03	y/D=2.11	0.08D

Table 3 Experimental parameters used for the acquisition of the PIV images

	# images	Delay time (μs)	Light sheet thickness (mm)
xy-planes			
Static case	1,000	2,000	1
Rotating case	1,000	350	1.5
yz-planes and *zx*-planes			
Static case	1,000	700	1.5
Rotating case	1,000	350	1.5

The light sheet, which is generated by a double cavity Nd:YAG LASER, has a pulse duration of 6 ns, a wavelength of 532 nm and a maximum energy per pulse of about 200 mJ. Seeding is made up of particles, whose diameter ranges from 1 to 20 μm, which scatter light at different wavelengths; it has, therefore, been possible to drastically reduce the spurious reflections with the use of a filter. To display, acquire and record digital images, the following items are used: a video camera Kodak Megaplus model ES 1.0 with a CCD sensor (1,008 × 1,018 pixels, 256 grey levels); a computer equipped with an acquisition board; a laser-acquisition system synchronizer. Table 3 reports, for both the static and the rotating cases, the principal experimental parameters used to acquire the PIV images relative to the three groups of planes associated to the three coordinate planes (*xy*, *yz*, *zx*).

The acquired images are processed by a high accuracy PIV iterative algorithm based on an image deformation method; the detailed description of the steps of the used PIV algorithm is reported in the work by Astarita and Cardone (2005). It has been verified through a statistical investigation that a sample of 1,000 images assures the statistical convergence of the three mean velocity components and of their fluctuations.

For the rotating case, the distributions of the mean velocity components have been obtained adopting two different procedures for *yz* and *xz* planes. For every investigated *yz*-plane (plane parallel to the rotation axis, Fig. 2), it has been necessary to acquire, in addition to the 1,000 images at $Re = 20,000$ and $Ro = 0.3$, 100 images with the same experimental parameters but with the fluid at rest. Indeed, the distributions of the velocity component w, with the channel in rotation, have been obtained by the following relation:

$$w(y, z) = w_1(y, z) - W_{2m} \qquad (3)$$

where w_1 is the mean flow field deduced by the images acquired at $Re = 20,000$ and $Ro = 0.3$, and W_{2m} is the velocity component evaluated by performing a spatial average of the mean (in time) velocity component w_2 distribution obtained from the images acquired with the rotating channel and with the fluid at rest. For the *xz*-investigated planes (plane normal to the rotation axis, Fig. 2), both the velocity components (u_1, w_1), obtained by the 1,000 images acquired at $Re = 20,000$ and $Ro = 0.3$, have been corrected. In this case, the distributions of the mean velocity components (u_2, w_2) relative to the 100 images acquired with the fluid at rest have been used to evaluate, by means of a minimization procedure, the coordinates (x_c, z_c) of the channel rotation centre. The knowledge of the rotation centre position (x_c, z_c) and of the angular speed ω allowed to subtract, for each point (x, z) of the investigated plane, the exact values of U_2 and W_2 that are the components of the rotation peripheral velocity V_{pp} (Fig. 3). Therefore, the correct velocity components (u, w) are evaluated by the following relations:
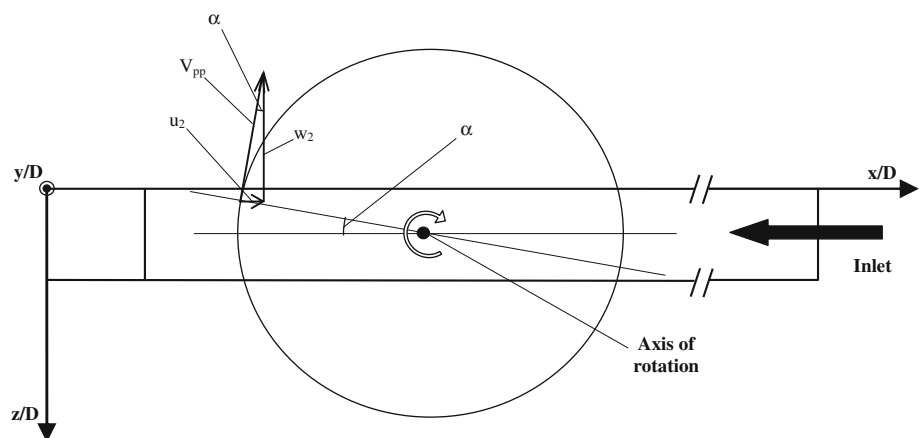
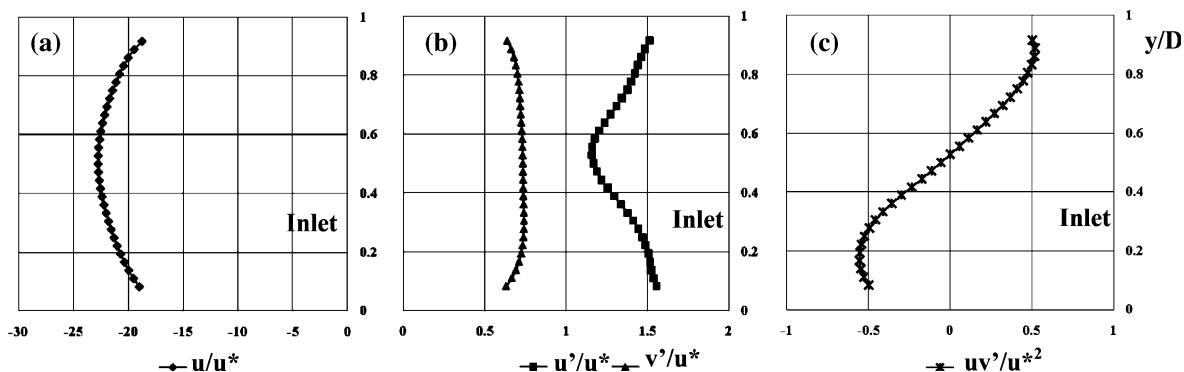$$u(x, z) = u_1(x, z) - U_2(x, z) \qquad (4)$$

$$w(x, z) = w_1(x, z) - W_2(x, z) \qquad (5)$$

where

$$U_2(x, z) = \omega \cdot \left(\sqrt{(x_c - x)^2 + (z_c - z)^2} \right) \cdot \sin(\alpha(x, z)) \qquad (6)$$

Fig. 3 Geometric scheme used for the correction of the velocity component distributions u and w relative to the *xz*-investigated planes (rotating case, $Re = 20,000$ and $Ro = 0.3$)

Fig. 4 Inlet flow conditions measured at $x/D = 3$ and $z/D = 0.5$ (static case, $Re = 20,000$): **a** profile of the axial velocity u/u^*, **b** profile of the turbulent intensities u'/u^* and v'/u^* and **c** profile of the Reynolds stresses $u'v'/u^{*2}$

$$W_2(x,z) = \omega \cdot \left(\sqrt{(x_c - x)^2 + (z_c - z)^2} \right) \cdot \cos(\alpha(x,z))$$
$$(7)$$

with

$$\alpha(x,z) = \text{arctg}\left(\frac{|z - z_c|}{|x - x_c|} \right) \tag{8}$$

3 3D reconstruction of the flow field and vortical field

In order to perform a 3D reconstruction of the mean flow and vortical fields in the two halves of the turn region and in the outlet duct, the three groups of mean velocity components distributions associated to the three coordinate planes (xy, yz, zx), previously filtered by a Wiener filter, have been interpolated on a common 3D grid. In this three-dimensional domain, the distributions of the three velocity components have been obtained by averaging the velocity components distributions that are in common to two of the planes groups mentioned earlier. Such velocity components (indicated with u_g, v_g and w_g) have been used to evaluate the module of the velocity V by means of the following relation.

$$V = \frac{\left(\sqrt{\left(u_g^2 + v_g^2 + w_g^2\right)} \right)}{U} \tag{9}$$

It has been also possible to evaluate the vorticity components Ω_x, Ω_y and Ω_z for all the slices parallel to the coordinate planes using the formulae based on the Stokes' theorem:

$$\Omega_l = \lim_{s \to 0} \oint_C \frac{V \cdot dl}{S} \tag{10}$$

where C is a square circuit formed by eight velocity points and containing the surface S that is normal to the l axis (Foucaut and Stanislas 2002). The calculation of Ω_x, Ω_y

and Ω_z allowed to plot the volumetric distributions of the vorticity module Ω (Eq. 11) in the investigated regions of the test channel both for the static and rotating case.

$$\Omega = \frac{\left(\sqrt{\left(\Omega_x^2 + \Omega_y^2 + \Omega_z^2\right)} \right) \cdot D}{U} \tag{11}$$

In the present work, the vortical field will be described by plotting, in the investigated regions of the channel, the iso-surfaces of the vorticity module. The vortex detection ability of the chosen criterion has been found to be, for the considered flow field, equivalent to the λ_2-criterion[1] (Jeong and Hussain (1995)). Indeed, in all the investigated regions of the channel, the iso-Ω and iso-λ_2 surfaces have detected the same vortical structures. It has been decided to plot the vorticity module because this quantity, for the investigated flow field, allows not only to perform a vortex detection but also to identify the high shear stress regions and to provide the relative importance of the different vortical structures.

4 Experimental results

In this section, the 3D mean vortical and flow fields relative to the second part of the turn region and to the outlet duct for the static case, and relative both to the whole turn region and to the outlet duct for the rotating case will be described. All the mean velocity components distributions shown in this section are normalized by means of the fluid mean velocity U.

In Fig. 4 are reported the profiles of the axial velocity components (u), the turbulence intensities (u' and v') and the Reynolds stresses (uv') measured in the inlet duct at $x/D = 3$ and $z/D = 0.5$ for the static case and non-dimensionalized on the wall friction velocity (u^*). They are

---

[1] The λ_2-criterion is a vortex identification method based on the eigenvalues of the sum of the strain and rotation square tensor.

only required for using the present experimental data as a tool to validate the computer programs developed to simulate these complex 3D flows.

Before beginning the discussion on the experimental results, it is needed to notice that the grid used to perform the 3D reconstruction of the flow field does not completely fill the measurement domain. For this reason, the vortical structures positioned very close to the channel walls either are not detected or are only partially visible in the 3D reconstructions of the mean flow and vortical fields. Furthermore, some vortical structures detected in the two-dimensional flow fields shown in this section, because of their small strength, are not visible in the 3D vorticity distributions.

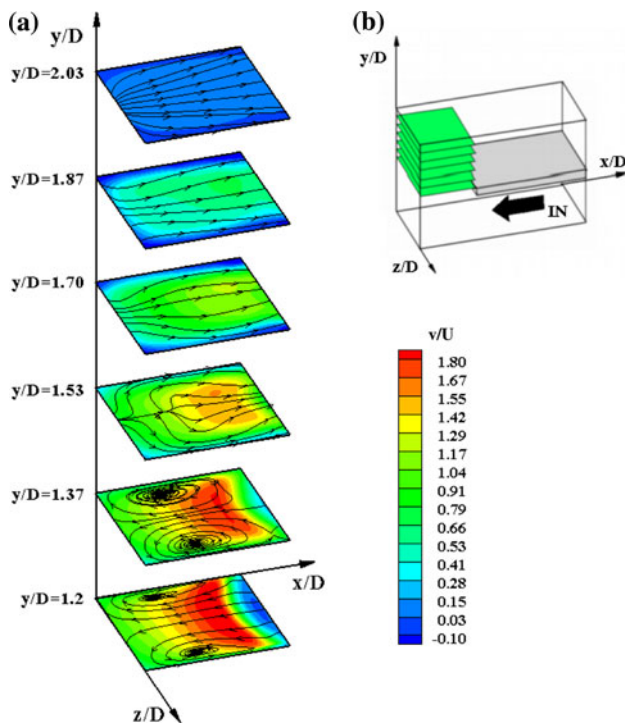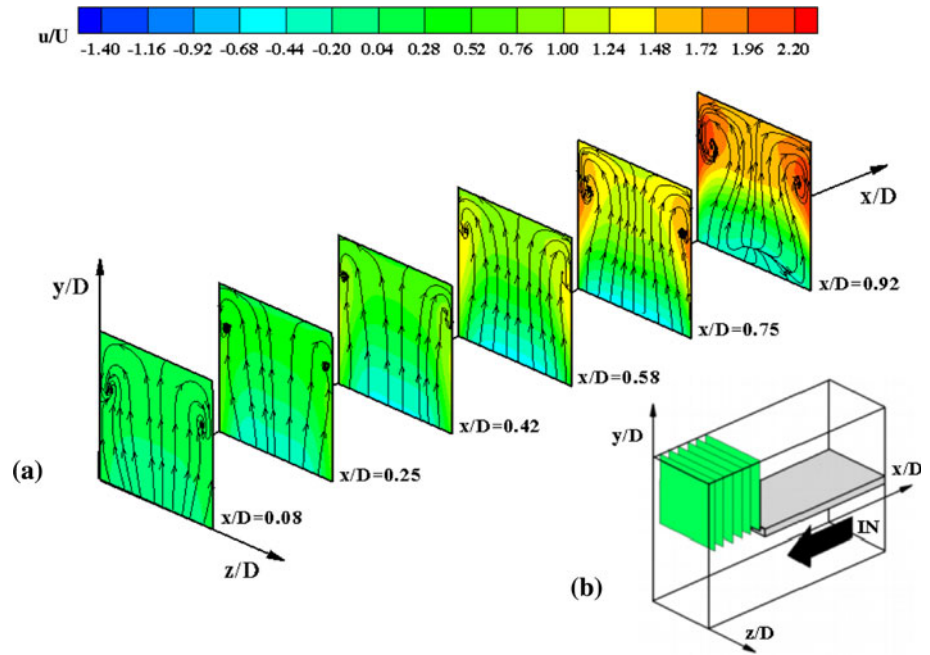### 4.1 Static case

4.1.1 Second half of the turn region

In Fig. 5 the iso-Ω surfaces relative to $\Omega = 2$ (Fig. 5b), $\Omega = 3.5$ (Fig. 5c) and $\Omega = 6.5$ (Fig. 5d) are reported. Figure 5b shows two iso-Ω surfaces (indicated by I), with an almost cylindrical shape, which start from the frontal wall and develop along the corners formed by the two side walls and by the external wall; these iso-Ω surfaces (I), along the flow direction, tend to get together with the two iso-Ω surfaces (indicated by II) that face to the two side walls. The first two iso-Ω surfaces (I) are associated to the vortices located along the corners formed by the two side walls and by the external wall of the second half of the turn region (Fig. 6). These vortices are a consequence of the impingement of the flow coming from the first part of the turn on the external wall of the second part of the turn region. Indeed, this impingement determines in the yz-planes a flow bifurcation and consequentially the formation of two symmetrical counter-rotating vortices. The other two iso-Ω surfaces (II) are due to the vortices ($y/D = 1.2$ and $y/D = 1.37$, Fig. 7) that develop as a consequence of the pressure gradient associated to the centrifugal forces present in the turn for the main flow curvature. These vortices are known in literature as Dean vortices. The shape of the two iso-Ω surfaces (II) near the two side walls (Fig. 5b) and the extinction of the Dean vortices near the external wall of the second half of the turn (Fig. 7) are evidence that these vortices bend and, as it will be shown in the next subsection, persist also in the outlet duct. The Dean vortices are stronger than the ones located along the corners formed by the two side walls and by the external wall of the second half of the turn. Indeed, from Fig. 5c, it is possible to see the extinction of the iso-Ω surfaces (I) in proximity of the frontal wall. By increasing the vorticity level (Fig. 5d), it is possible to notice that the iso-Ω surfaces tend to collapse on the tip of the partition wall where the shear stresses are strongest.
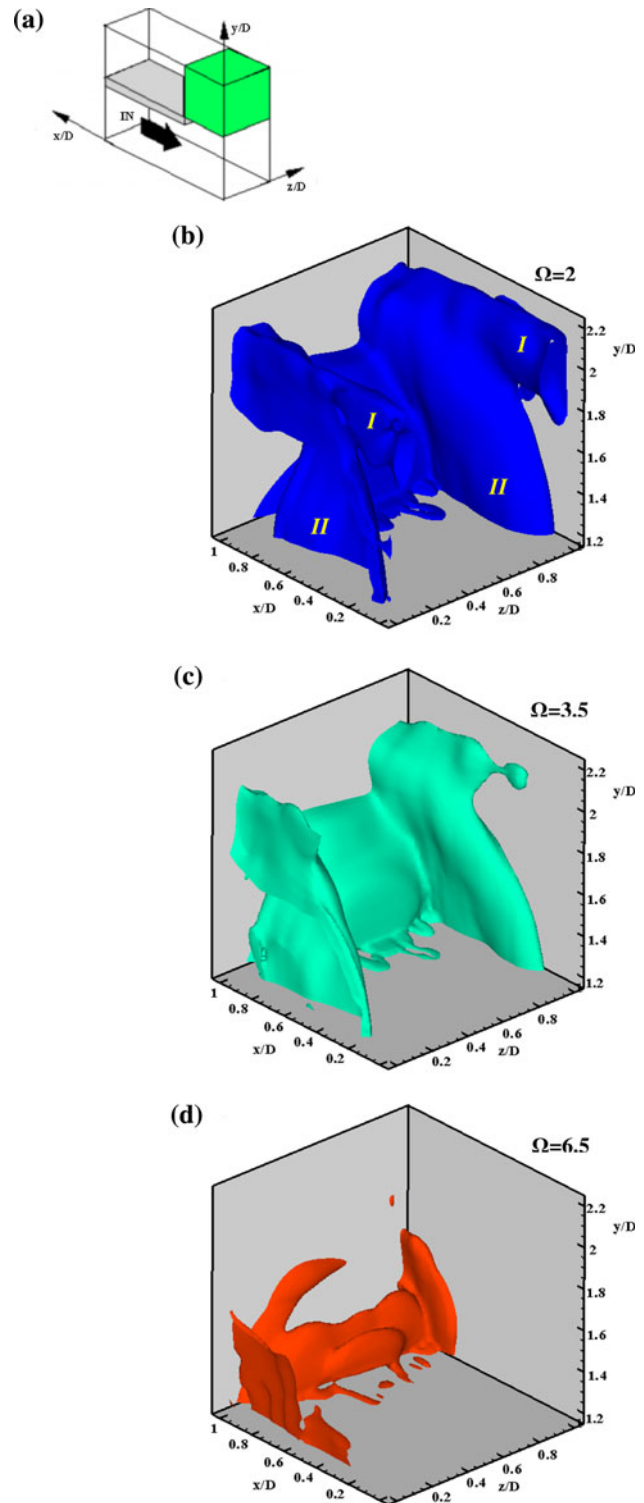
Fig. 5 3D reconstruction of the vorticity distribution in the second half of the turn (static case, $Re = 20,000$): **a** sketch of the test region, **b** iso-Ω surfaces ($\Omega = 2$), **c** iso-Ω surfaces ($\Omega = 3.5$) and **d** iso-Ω surfaces ($\Omega = 6.5$)
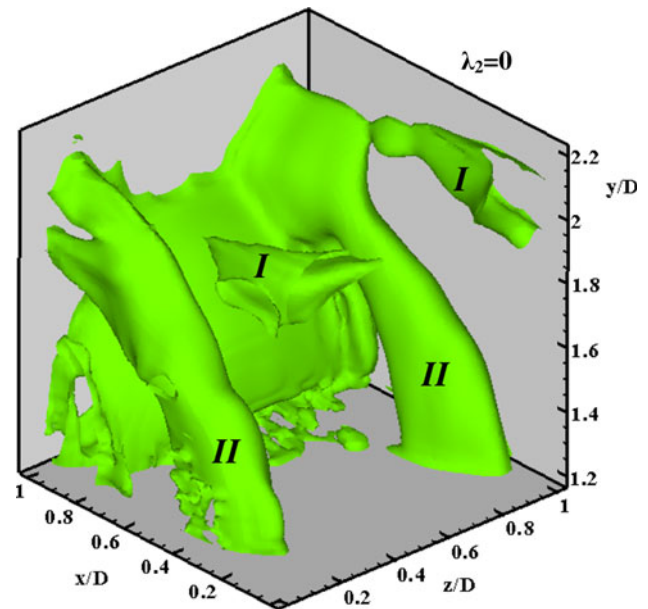
In order to compare the two vortex detection methods discussed in Sect. 3, in Fig. 8, the iso-λ_2 surfaces relative to the second half of the turn region are reported.

Fig. 6 Secondary flow fields measured in the second half of the turn (static case, $Re = 20,000$): **a** distributions of the mean plane-normal velocity component u/U with the streamlines superimposed and **b** sketch of the test region with the yz-investigated planes

Fig. 7 Secondary flow fields measured in the second half of the turn (static case, $Re = 20,000$): **a** distributions of the mean plane-normal velocity component v/U with the streamlines superimposed and **b** sketch of the test region with the xz-investigated planes


Fig. 8 Iso-λ_2 surfaces relative in the second half of the turn (static case, $Re = 20,000$). The view point of the investigated region is reported in Fig. 5a

A comparison between the iso-λ_2 (Fig. 8) and the iso-Ω (Fig. 5b) shows that both methods detect the same vortical structures. Nevertheless, as expected, the iso-λ_2 criterion enables to clearly identify the vortices, while the vorticity mixes them with regions of high shear stresses. In reality,

close to the side walls, the vorticity criterion highlights both vortical and shear stress regions (compare the iso-λ_2 and iso-Ω surfaces denoted with *II* in Figs. 5, 8, respectively). The inspection of the iso-λ_2 contours, conducted in all the investigated regions of the channel both for the static and the rotating cases, allowed to discern the iso-Ω surfaces associated to vortical structures from the ones relative to high shear stress zones. In this work, the vortical field will be described by using the iso-Ω surfaces for the
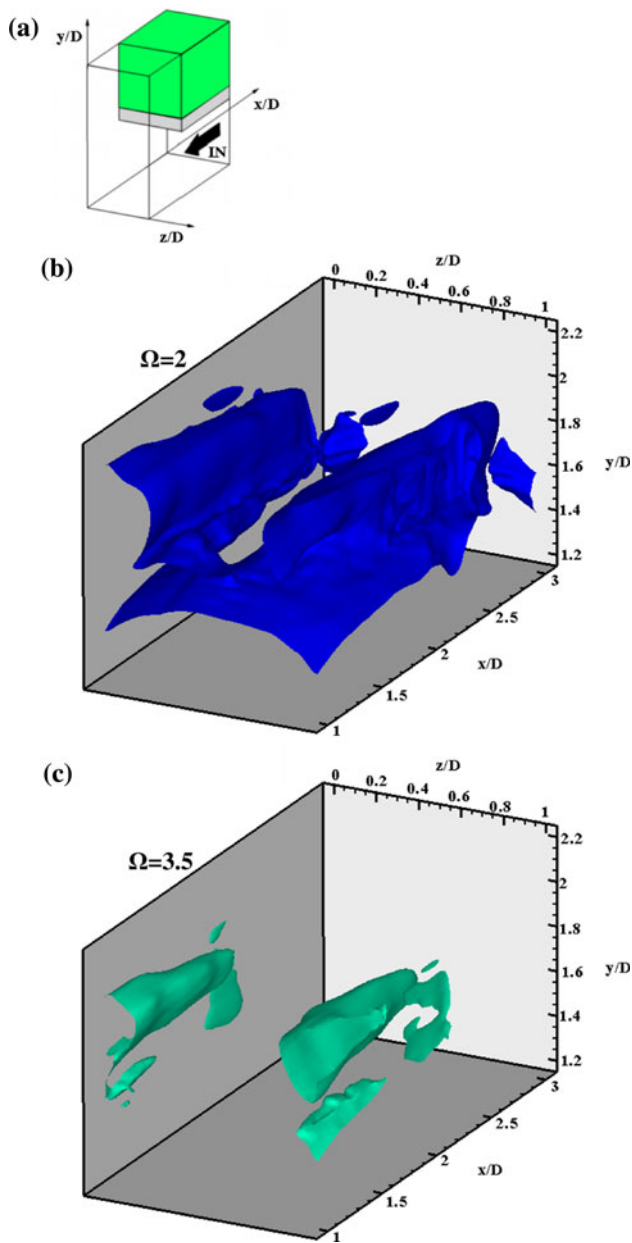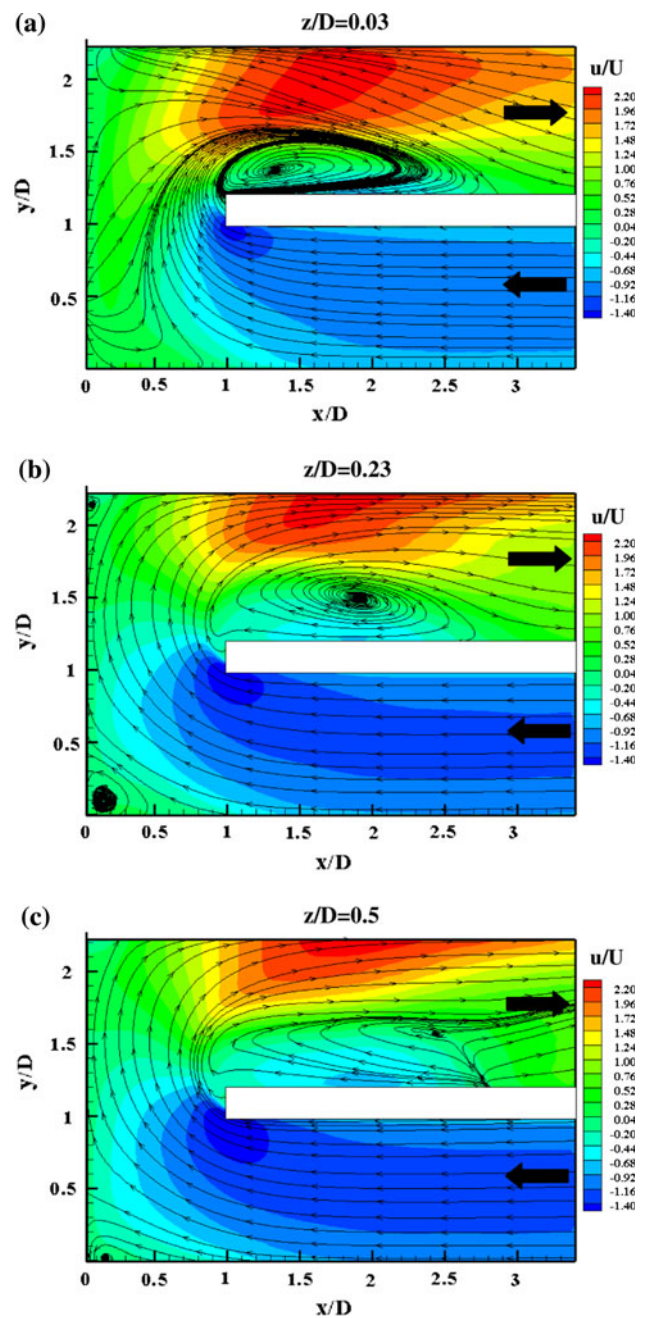
Fig. 9 3D reconstruction of the vorticity distribution in the outlet duct (static case, $Re = 20,000$): **a** sketch of the test region, **b** iso-Ω surfaces ($\Omega = 2$) and **c** iso-Ω surfaces ($\Omega = 3.5$)


Fig. 10 Distributions of the mean velocity component u/U with the streamlines superimposed (static case, $Re = 20,000$): **a** $z/D = 0.03$, **b** $z/D = 0.23$ and **c** $z/D = 0.5$

motivations reported in the last paragraph of the Sect. 3 and for sake of brevity, no more iso-λ_2 surfaces will be shown in the following.

4.1.2 Outlet duct

In Fig. 9, the iso-Ω surfaces relative to the outlet duct, corresponding to Ω equal to 2 (Fig. 9b) and 3.5 (Fig. 9c) are reported. In order to simplify the description of the complex 3D flow field, the main flow fields (xy-planes) relative to three different planes (Fig. 10) and the

secondary flow fields relative to the all yz-planes investigated in the outlet duct (Fig. 11) are also shown.

The Dean vortices persist also in the outlet duct; indeed, from Fig. 9c, it is possible to see near the external wall, two iso-Ω surfaces having an almost cylindrical shape and facing the two side walls. When the Ω level is decreased (Fig. 9b), in addition to the two iso-Ω surfaces associated to the Dean vortices, it is possible to see an iso-Ω surface with the concavity directed towards the partition wall. The shape

Fig. 11 Secondary flow fields measured in the outlet duct (static case, $Re = 20,000$): **a** distributions of the mean plane-normal velocity component u/U with the streamlines superimposed ($1 \leq x/D \leq 1.83$), **c** distributions of the mean plane-normal velocity component u/U with the streamlines superimposed ($2 \leq x/D \leq 3$) **b** and **d** sketch of the test region with the yz-investigated planes
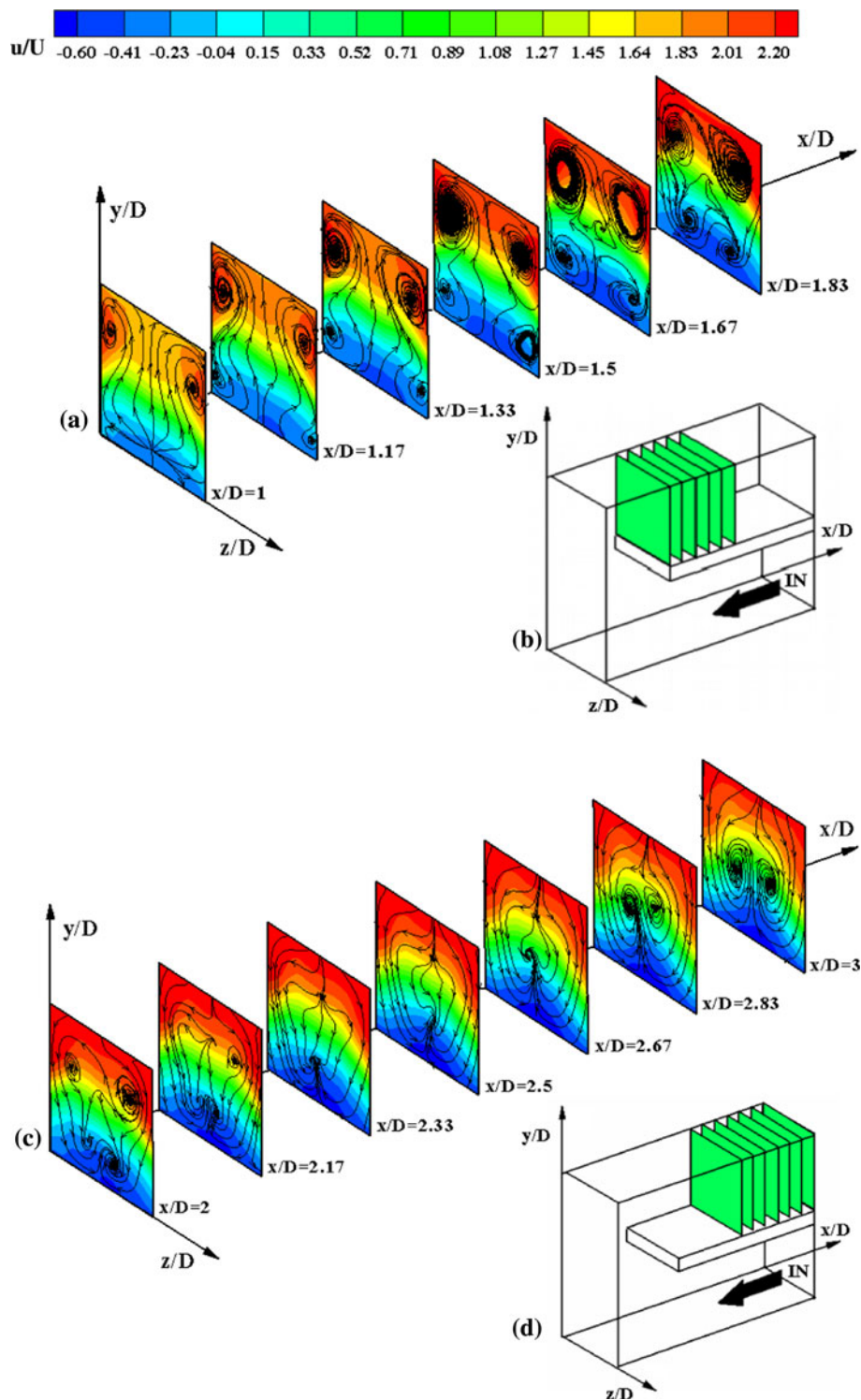

and position of this iso-Ω surface allow to associate it to the high shear stresses present on the boundary of the large recirculation bubble positioned near the partition wall of the outlet duct, immediately after the turn region (Fig. 10).

The main flow field measured in the plane $z/D = 0.03$ (Fig. 10a) shows, in the outlet duct, a reattachment zone

near the partition wall at about 1.5 hydraulic diameters from the exit section of the turn. By moving the investigated planes from the side wall towards the symmetry plane (Fig. 10b, c), it is possible to observe that the centre of the recirculation bubble moves downstream and slightly towards the central part of the duct; moreover, the

Fig. 12 3D reconstruction of the flow field in the outlet duct (static case, $Re = 20,000$): **a** 3D streamlines and **b** sketch of the test region
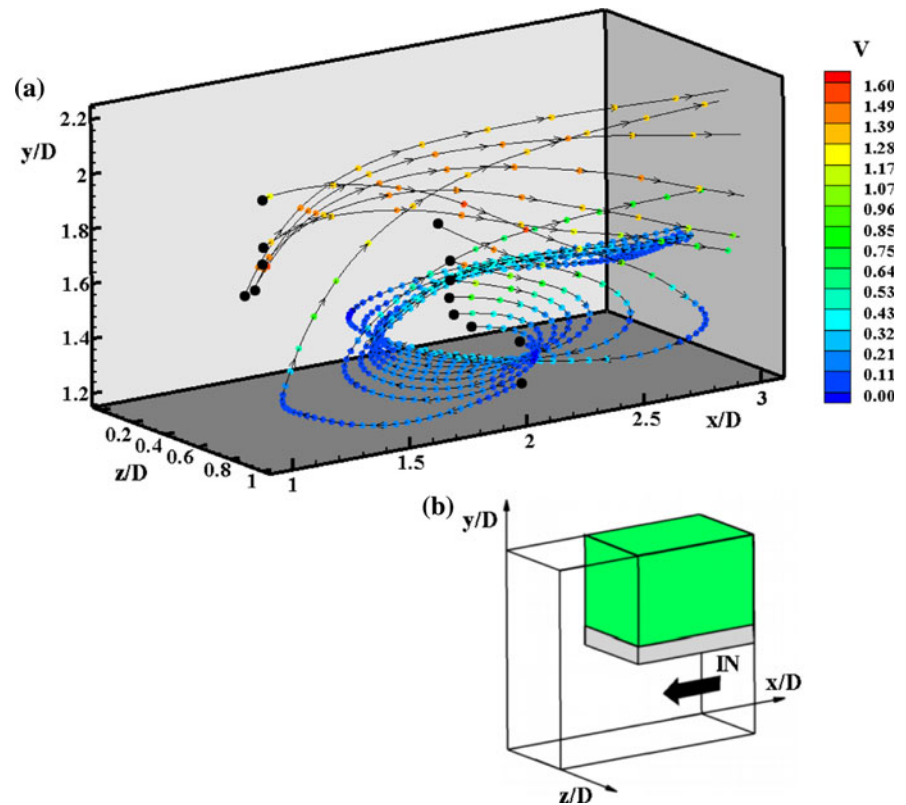
reattachment zone is replaced by a "*linear source*" slightly sloping upstream. For the mass continuity, this "*linear source*" is justified by the impingement, in proximity of the partition wall, between two opposite secondary flows that generate, downstream and upstream of the "*linear source*", two different flow field evolutions whose understanding could be facilitated by the detailed analysis of the secondary flow fields in the outlet duct (Fig. 11).

In the investigated planes located near the tip of the partition wall (Fig. 11a), the flow field is marked by the presence, near the external wall, of two counter-rotating vortices representative of the Dean vortices. Along the flow direction, these vortices tend to push the fluid along the two side walls towards the partition wall where the phenomenon of the reattachment occurs ($1.83 \leq x/D \leq 2.17$, Fig. 11a and c) and, at the same time, it is also possible to observe a gradual decrease of their strength. Indeed in the subsequent planes ($2.33 \leq x/D \leq 2.67$, Fig. 11c), the secondary flow field is marked by two symmetrical flows that start from the external wall and after flowing along the two side walls join again in proximity of the partition wall. The junction of these two flows promotes the formation, downstream of the plane $x/D = 2.5$, of two weak counter-rotating vortices positioned at the centre of the section (Fig. 11c). On the other hand, upstream of the plane $x/D = 2.5$ two counter-rotating vortices that along the

opposite direction to the main flow tend to shift their centre towards the inner corners and to drastically reduce their size in proximity of the tip of the partition wall are present (Fig. 11a). These two last vortices constitute the large recirculation bubble mentioned earlier. This bubble is therefore formed by two lobes both characterized by one vortex having axis parallel to the partition wall and sloping to the side wall (Fig. 12 and Animation 1). In order to make the understanding of the flow field easier, Fig. 12 reports the entire investigated volume of the outlet duct but, since the flow field is symmetrical, only the streamlines relative to a half of the duct are drawn.

The secondary flow field measured at the exit of the turn section ($x/D = 1$, Fig. 11a) shows a source positioned near the partition wall and generated by the impingement between the reverse flow of the large recirculation bubble present in the outlet duct and the main flow passing through the second half of the turn.

## 4.2 Rotating case

4.2.1 First half of the turn region

Figure 13 reports the iso-Ω surfaces corresponding to $\Omega = 4.5$ and the streamlines relative to the first half of the turn. The more significant aspect that has to be highlighted
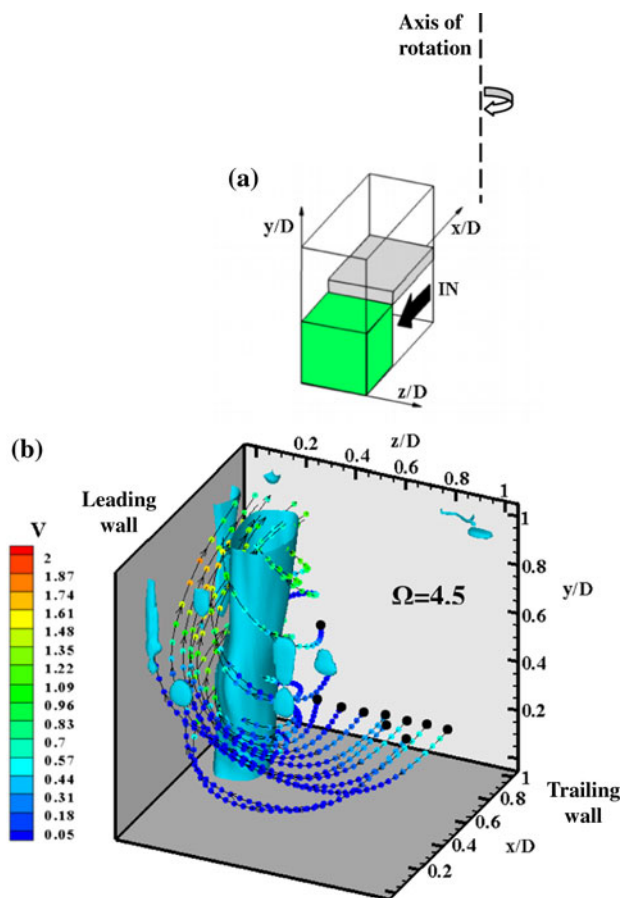
Fig. 13 3D reconstruction of the vorticity distribution in the first half of the turn (rotating case, $Re = 20{,}000$ and $Ro = 0.3$): **a** sketch of the test region, **b** iso-Ω surfaces ($\Omega = 4.5$) and streamlines

is the presence of a cylindrical iso-Ω surface that extends near the leading wall (Fig. 13b). As shown by the streamlines, this iso-Ω surface is linked to the presence, near the leading wall of the first part of the turn, of a strong vortex. To understand the genesis of this vortex, it is necessary to know the behaviour of the flow in the inlet duct. In this region, the Coriolis force promotes the formation of secondary flows constituted by two counter-rotating cells. The convection associated to these secondary
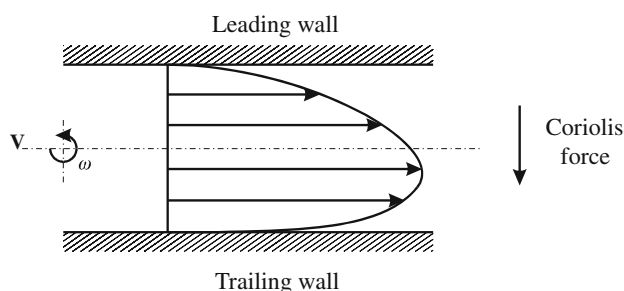
Fig. 14 Sketch of the axial velocity profile (*inlet duct*)

flows shifts the peak value of the axial velocity towards the trailing wall (Fig. 14), which is also known in literature as unstable wall or pressure side (Qin and Pletcher (2006)). Therefore, the flow from the inlet duct, in the first half of the turn, bumps against the frontal wall near the trailing wall then moves, along the frontal wall, towards the leading wall and finally comes back towards the inlet of the turn (see streamlines, Fig 13b and Animation 2) forming the strong vortex.

4.2.2 Second half of the turn region

For both to follow the evolution of the vortical structures identified in the whole turn region and to provide an overall view of the vortical field in all the detected regions of the test channel, in Fig. 15, the iso-Ω surfaces ($\Omega = 4.5$) relative to the outlet duct and to the whole turn region have been reported. Also for the rotating case in the second half of the turn, the flow coming from the first half bumps against the external wall. In this case, because of the channel rotation, the bifurcation zone is shifted towards the trailing wall, and this produces two asymmetric counter-rotating vortices positioned in proximity of the corners formed by the external wall and by the leading and trailing walls (Fig. 16). These vortices are identified in the 3D reconstruction of the vorticity module Ω (Fig. 15b) by the two closed iso-surfaces that start from the frontal wall and extend along the two external corners.

The large vortex positioned near the leading wall in the first half of the turn, in the second half bends towards the trailing wall (Fig. 15b) as the Coriolis force becomes equal to zero in the turn region. This phenomenon determines a strong impinging flow on the trailing wall towards the outlet section of the turn (Fig. 16a, $x/D = 0.83$). The part of the impinging flow going upwards moves towards the leading wall wrapping the vortex located near the corner formed by the external and leading wall and generating, in the plane, a new vortex with the same direction of rotation of the previous one and shifted towards the trailing wall. The part of the impinging flow directed towards the partition wall supports the vortex located near the lower corner of the trailing wall that, as it will be shown in the next subsection, constitutes the asymmetric recirculation bubble present immediately after the turn region near the partition wall of the outlet duct. This recirculation bubble is bounded by a high shear stress region that is detected, in Fig. 15b, by the iso-Ω surface positioned between the outlet section of the turn and the larger cylindrical surface. Indeed, in the outlet duct, moving the xy-investigated planes from the leading to the trailing wall (Fig. 17), it can be observed that the recirculation bubble tends to move upstream entering in the turn region in proximity of the trailing wall.

Fig. 15 3D reconstruction of the vorticity distribution in the whole turn and in the outlet duct (rotating case, $Re = 20,000$ and $Ro = 0.3$): **a** sketch of the test region and **b** iso-Ω surfaces ($\Omega = 4.5$)
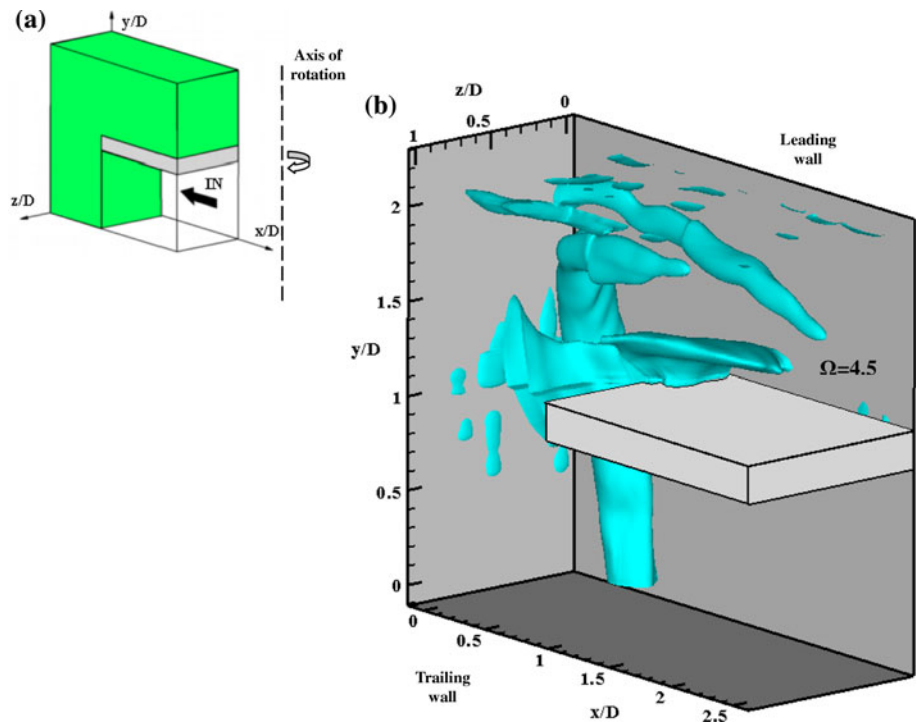

Fig. 16 Secondary flow fields measured in the second half of the turn (rotating case, $Re = 20,000$ and $Ro = 0.3$): **a** distributions of the mean plane-normal velocity component u/U with the streamlines superimposed and **b** sketch of the test region with the yz-investigated planes
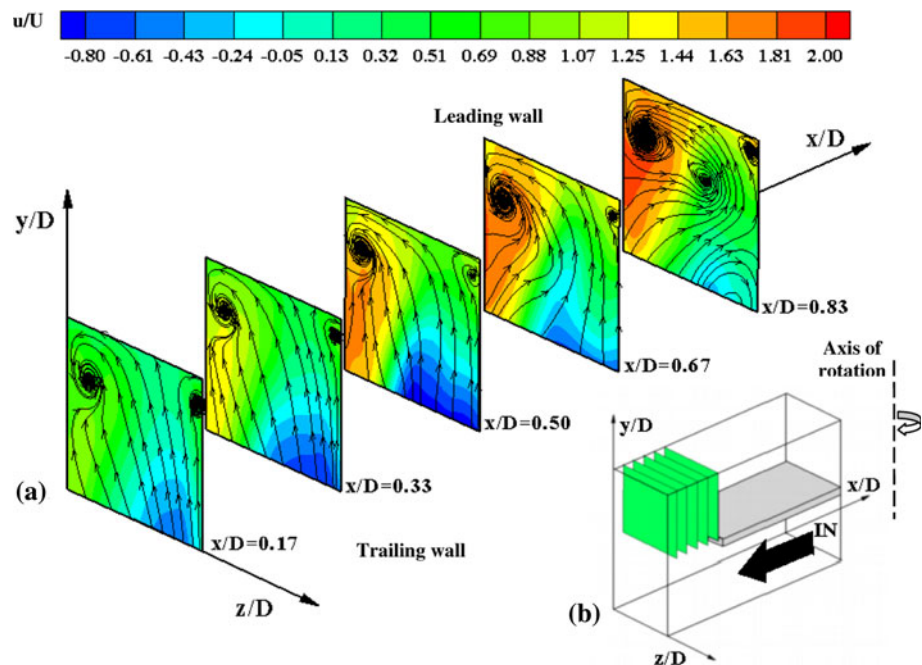
4.2.3 Outlet duct

In the 3D reconstruction of the mean vortical field (Fig. 15), the two co-rotating vortices, forming the large vortical structure positioned at the exit of the turn near the external wall ($x/D = 1$, Fig. 18a), are detected by the

two large iso-Ω surfaces with an almost cylindrical shape that are positioned near the leading and the trailing wall towards the external wall. These two iso-Ω surfaces show a different evolution along the flow direction; indeed, the vortex positioned near the trailing wall has, for $\Omega = 4.5$, a reduced extension with respect to the one positioned
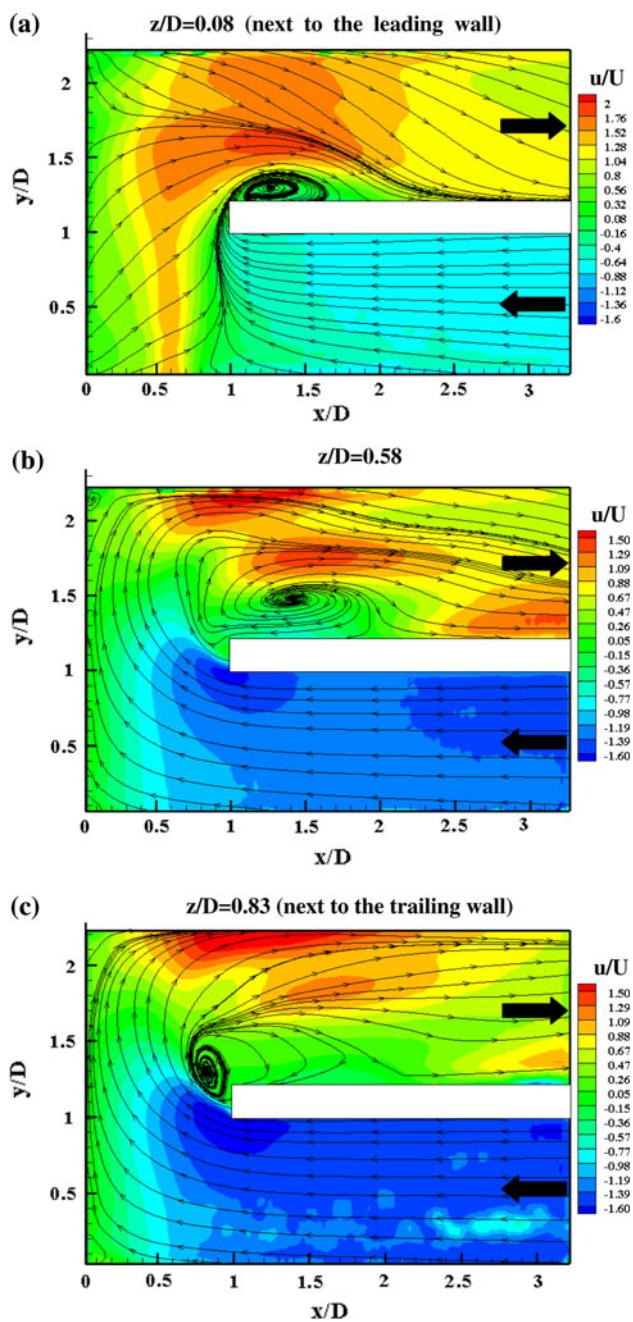
Fig. 17 Distributions of the mean velocity component u/U with the streamlines superimposed (rotating case, $Re = 20{,}000$ and $Ro = 0.3$): **a** $z/D = 0.08$, **b** $z/D = 0.58$ and **c** $z/D = 0.83$

near the leading wall that has a more slender shape and tends to tilt towards the partition wall. The different behaviours of these two vortices could be due to the asymmetric configuration of the large recirculation bubble, present near the partition wall of the outlet duct immediately after turn region (Fig. 17), and identified by the iso-Ω surface positioned in the lower part of the outlet duct.

In order to facilitate the understanding of the genesis of the asymmetric recirculation bubble, some preliminary observations will be done. As already asserted in the Sect. 4.2.1, for radially outward flow, the Coriolis force determines an asymmetry in the axial velocity profile (Fig. 14); indeed, the fluid with higher velocity is pushed towards the trailing wall that is also called the pressure side, whereas for radially inward flow the Coriolis force acts in the opposite direction so the leading wall becomes the pressure side. In the first part of the outlet duct characterized by the presence, near the partition wall, of the recirculation bubble, the Coriolis force acts both towards the leading wall (in proximity of the external wall) and towards the trailing wall (in proximity of the partition wall). Indeed, the flow in proximity of the external wall of the outlet duct, being radially inward directed, is pushed by the Coriolis force from the trailing to the leading wall (see the direction of the streamlines in proximity of the external wall, Fig. 18a and c). As described in the Sect. 4.1.2, in the static case, the large recirculation bubble downstream of the turn region is characterized by a reverse flow formed by two counter-rotating vortices positioned near the two inner corners (Fig. 11a). With the rotation of the channel and consequently with the main action of the Coriolis force directed, near the partition wall, from the leading to the trailing wall, it is possible to observe a strong increase of the size of the vortex positioned near the corner between the trailing wall and the partition wall (Fig. 18a and Animation 3) at expense of the other one. Furthermore, this vortex, forming the large recirculation bubble, is pushed upstream towards the second half of the turn region by the centrifugal force due to the channel rotation (Fig. 17c). The passage from the symmetrical configuration of the recirculation bubble (static case) to the asymmetric one (rotating case) is associated, at the same time, to the formation of a low pressure zone in the corner formed by the leading and the partition wall. Indeed, since the reverse flow of the recirculation bubble of the outlet duct is radially outward directed, the lower part of the leading wall, owing to the action of the Coriolis force, becomes a low pressure zone promoting the bending towards the partition wall of the slender vortex positioned in the outlet duct close to the leading wall (Fig. 15). For $x/D \geq 1.67$ (Fig. 18a and c), it is possible to observe, in proximity of the lower part of the trailing wall, the extinction of the vortex forming the asymmetric recirculation bubble that occurs after the birth of another vortex, with direction of rotation opposite to the previous one. The latter vortex gives rise, together with the other vortex positioned near the higher part of the trailing wall, to a vortical structure formed by two co-rotating vortices characterizing the whole secondary flow field for $x/D > 2$.

Fig. 18 Secondary flow fields measured in the outlet duct (rotating case, $Re = 20,000$ and $Ro = 0.3$): **a** distributions of the mean plane-normal velocity component u/U with the streamlines superimposed ($1 \leq x/D \leq 1.67$), **c** distributions of the mean plane-normal velocity component u/U with the streamlines superimposed ($1.83 \leq x/D \leq 2.5$), **b** and **d** sketch of the test region with the yz-investigated planes
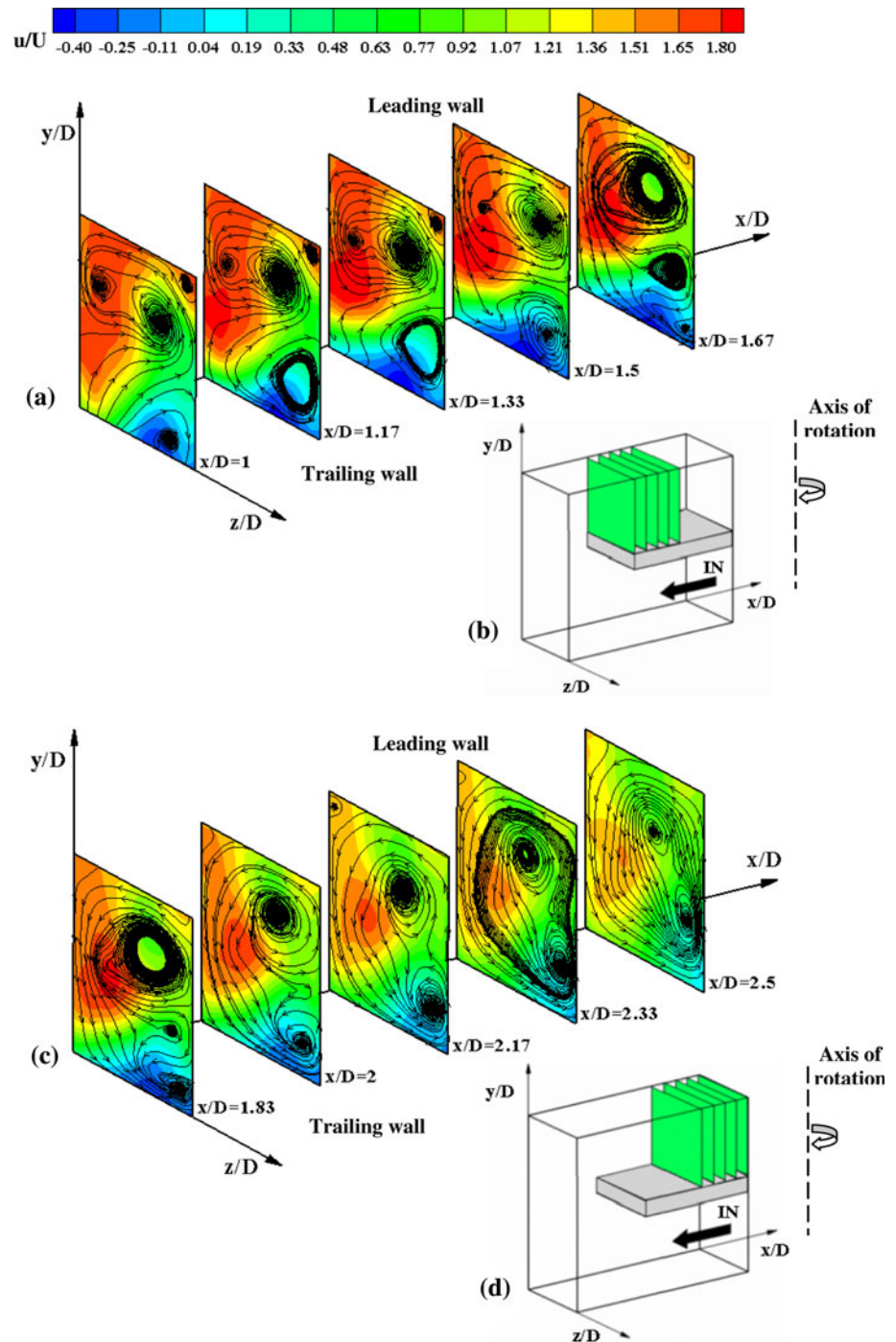
5 Conclusions

PIV measurements have been performed in a channel with a sharp "U" turn with the aim to both obtain detailed information about the main and the secondary flow fields and to realize a 3D reconstruction of the mean flow and vortical field, with and without rotation.

For the static case, in the second part of the turn region, it has been observed that the flow field is characterized by the presence of two couples of counter-rotating vortices. The first couple, located along the corners formed by the two side walls and by the external wall, is generated by the impingement of the flow, coming from the first half of the turn, on the external wall of the second half. The second couple, stronger than the first one and known in literature as Dean vortices, is generated by the pressure gradient associated to the centrifugal forces due to the main flow curvature at the turn and persists also in the outlet duct.

Immediately after the turn, the large recirculation bubble positioned on the partition wall of the outlet duct is formed by two lobes both characterized by one vortex having axis parallel to the partition wall and sloping to the side wall. Downstream of the reattachment zone present on the partition wall of the outlet duct, the secondary flow field is marked by two counter-rotating vortices positioned at the centre of the cross section.

For the rotating case, in the first half of the turn it has been observed that the flow field is marked by the presence of a strong vortex that develops along the leading wall. In the second half of the turn, this vortex undergoes a curvature towards the trailing wall. The rotation determines an asymmetry both of the couple of vortices positioned, in the second half of the turn, along the external corners and of the recirculation bubble located near the partition wall of the outlet duct. In particular, this recirculation bubble is formed by only one vortex that extends along the corner formed by the trailing wall and the partition wall. Downstream of the recirculation bubble, the secondary flow fields are marked by the presence of only one vortical structure formed by two co-rotating vortices shifted towards the trailing wall.

References

Al-Qahtani M, Jang Y-J, Chen H-C, Han J-C (2002) Flow and heat transfer in rotating two-pass rectangular channels (AR = 2) by Reynolds stress turbulence model. Int J Heat Mass Transf 45:1823–1838

Arts T, Lambert de Rouvroit M, Rau G, Acton P (1992) Aero-thermal investigation of the flow developing in a 180 degree turn channel. Proceedings of international symposium on heat transfer in turbomachinery, Athens

Astarita T, Cardone G (2005) Analysis of interpolation schemes for image deformation methods in PIV. Exp Fluids 38:233–243

Brossard C, Servouze Y, Gicquel P, Barrier R (2005) Characterization of the flow field inside a rotating, rib-roughened, U-shaped channel using particle image velocimetry. In: Proceedings of 21st international congress instrumentation in aerospace simulation facilities

Cheah SC, Iacovides H, Jackson DC, Ji H, Launder BE (1996) LDA investigation of the flow development through rotating U-ducts. J Turbomach 118:590–596

Foucaut JM, Stanislas M (2002) Some considerations on the accuracy and frequency response of some derivative filters applied to particle image velocimetry vector fields. Meas Sci Technol 13:1058–1071

Iacovides H, Raisee M (1999) Recent progress in the computation of flow and heat transfer in internal cooling passages of turbine blades. Int J Heat Fluid Flow 20:320–328

Iacovides H, Launder BE, Li H-Y (1996) The computation of the flow development through stationary and rotating U-ducts of strong curvature. Int J Heat Fluid Flow 17:22–33

Iacovides H, Jackson DC, Kelemenis G, Launder BE, Yuan YM (1999) Experiments on local heat transfer in a rotating square-ended U-bend. Int J Heat Fluid Flow 20:302–310

Jeong J, Hussain F (1995) On the identification of a vortex. J Fluid Mech 285:69–94

Kim KM, Kim YY, Lee DH, Rhee DH, Cho HH (2007) Influence of duct aspect ratio on heat/mass transfer in coolant passages with rotation. Int J Heat Fluid Flow 28:357–373

Kiml R, Mochizuki S, Murata A (1998) Influence of 180 degree sharp turn on the heat transfer and flow behavior in a smooth square cross sectional serpentine channel. In: Proceedings of 8th international symposium on flow visualizations

Kline SC, McClintok FA (1953) Describing uncertainties in single-sample experiment. Mech Eng 75:3–8

Liou TM, Chen C–C (1999a) LDV study of the developing flows through a smooth duct with a 180 deg straight-corner turn. J Turbomach 121:167–174

Liou TM, Chen C–C (1999b) Heat transfer in a rotating two-pass smooth passage with a 180° rectangular turn. Int J Heat Mass Transf 42:231–247

Murata A, Mochizuki S (2004) Large eddy simulation of turbulent heat transfer in a rotating two-pass smooth square channel with sharp 180° turns. Int J Heat Mass Transf 47:683–698

Qin Z, Pletcher RH (2006) Large eddy simulation of turbulent heat transfer in a rotating square duct. Int J Heat Fluid Flow 27:371–390

Schabacker J, Bolcs A, Johnson BV (1998) PIV investigation of the flow characteristics in an internal coolant passage with two ducts connected by a sharp 180° bend. ASME Preprint 98-GT-544, Stockholm, Sweden

Son SY, Kihm KD, Han J-C (2002) PIV flow measurements for heat transfer characterization in two-pass square channels with smooth and 90° ribbed walls. Int J Heat Mass Transf 45:4809–4822

Su G, Chen H-C, Han J-C, Heidmann JD (2004) Computation of flow and heat transfer in rotating channels (AR = 1:1, 1:2, and 1:4) with smooth walls by a Reynolds stress turbulence model. Int J Heat Mass Transf 47:5665–5683

Wang TS, Chyu MK (1992) Influence of turning geometry on convective transport in a square duct with a 180–deg sharp turn. Proceedings of international symposium on heat transfer in turbomachinery, Athens